https://doi.org/10.5194/egusphere-2025-229
Preprint. Discussion started: 17 March 2025

Influencing Factors of Gas-Particle Distribution of Oxygenated Organic Molecules in Urban Atmosphere and Its Deviation from Equilibrium Partitioning

Xinyu Wang[1], Nan Chen[2,3], Bo Zhu[2,3], Huan Yu[1,2] *

[1] School of Environmental Studies, China University of Geosciences, Wuhan, 430074, China

[2] Research Centre for Complex Air Pollution of Hubei Province, Wuhan 430074, China

[3] Hubei Ecological Environment Monitoring Center Station, Wuhan 430070, China

* Correspondence to: Huan Yu, yuhuan@cug.edu.cn

Abstract

Gas-to-particle partitioning governs the fate of Oxygenated Organic Molecules (OOMs) and the formation of organic aerosols. We employed a Chemical Ionization Mass Spectrometer equipped with a Filter Inlet for Gases and AEROsol (FIGAERO-CIMS) to measure gas-particle distribution of OOMs in a winter campaign in urban atmosphere. The observed gas to particle (G/P) ratios show a narrower range than the equilibrium G/P ratios predicted from saturation mass concentration C^* and organic aerosol content. The difference between observed and equilibrium G/P ratios could be up to 10 orders of magnitude, depending on C^* parameterization selection. Our random forest models identified relative humidity (RH), aerosol liquid water content (LWC), temperature and ozone as four influential factors driving the deviations of partitioning from equilibrium state. Random forest models with satisfactory performance were developed to predict the observed G/P ratios. Intrinsic molecule features far outweigh meteorological and chemical composition features in the model's predictions. For a given OOM species, particle chemical composition features including pH, RH, LWC, organic carbon, potassium and sulfate dominate over meteorological and gaseous chemical composition features in predicting the G/P ratios. We identified positive or negative effects, as well as the sensitive ranges, of these influential features using SHapley Additive exPlanations (SHAP) analysis and curve fitting with a generalized additive model (GAM). Our models found that temperature does not emerge as a significant factor influencing the observed G/P ratios, suggesting that other factors, most likely associated with particle composition, inhibit the

https://doi.org/10.5194/egusphere-2025-229
Preprint. Discussion started: 17 March 2025

gas/particle partitioning of OOMs in response to temperature change.

1. Introduction

Oxygenated organic molecules (OOMs) are ubiquitous in the atmosphere. They are key constituents of organic aerosols (OA) and play a critical role in particle formation and growth (Yuan et al., 2024). The distribution of an OOM between gas and particle phases not only reflects its volatility or water solubility, but also governs its formation pathways, atmospheric transport and deposition. Therefore, understanding the phase distribution of OOMs is essential for gaining insights into their volatility, transformation processes and environmental impacts in the atmosphere.

Gas-to-Particle (G/P) ratios of OOMs measured by laboratory (e.g., ozonolysis products from Δ^3-Carene (Li et al., 2024)) or field studies (e.g., in Hyytiälä forest, Finland (Lutz et al., 2019)) were sometimes used to derive saturation mass concentrations (C^*) or partitioning coefficients (K_i), assuming that the observed G/P ratios represent an equilibrium partitioning state (Priestley et al., 2024; Li et al., 2024; Lutz et al., 2019; Stark et al., 2017). However, the G/P ratio of an OOM in atmospheric conditions is influenced by not only intrinsic OOM physicochemical properties but also external factors such as meteorological shifts (Hildebrandt et al., 2009), precursor oxidation (Pankow, 1994; Seinfeld and Pankow, 2003), particle chemical composition, morphology and particle-phase reactions (Jang et al., 2002; George et al., 2007). As a result, OOMs rarely achieve equilibrium partitioning between the gas and particle phases (Roldin et al., 2014).

Gas/particle partitioning kinetics has been incorporated into many atmospheric aerosol models, such as aerosol dynamics models (Liu et al., 2019; Zaveri et al., 2014) and kinetic multilayer models (Fowler et al., 2018; Roldin et al., 2014), which accounted for molecular transfer rates, interphase interactions, and environmental variability (Shiraiwa and Pöschl, 2021) in the gas-to-particle transfer process. The development of these models has advanced our understanding of the distribution and transport of organic compounds. However, existing theories and models often rely on parameter simplifications or assumptions, and there is a lack of systematic studies examining the factors influencing the phase distribution of OOMs under real atmospheric conditions. In recent years, machine learning methods have been successfully applied to for a variety of purposes including compound identification (Franklin et al., 2022; Boiko et al., 2022), aerosol classification

https://doi.org/10.5194/egusphere-2025-229
Preprint. Discussion started: 17 March 2025

(Christopoulos et al., 2018; Bland et al., 2022), precursor apportionment (Pande et al., 2022; Wang et al., 2021) and property prediction (Gong et al., 2022; Ruiz-Jimenez et al., 2021). Machine learning has been proven to be a powerful, data-driven approach capable of uncovering complex and nonlinear relationships between variables. (Lin et al., 2022; Zhu et al., 2019). Unlike physical or chemical models, machine learning does not rely on predefined assumptions or simplifications, which enables it to unveil previously unrecognized interactions.

In this work, we employed a Chemical Ionization Mass Spectrometer equipped with a Chemical Ionization Mass Spectrometer equipped with a Filter Inlet for Gases and AEROsol (FIGAERO-CIMS) in an urban location to measure the concentrations of OOMs in both the gas and particle phases. By building data-driven machine learning models with the G/P ratio as the target variable, we explored the influencing factors of gas-particle distribution of OOMs and examined the factors that contribute to the deviations from equilibrium gas/particle partitioning. This study offered new insights and provided the foundation for future studies on the atmospheric behavior of OOMs.

2. Methodology

2.1 OOM measurement

Hourly measurements of OOMs in both gas and particle phases was conducted during a winter campaign from December 5th, 2022, to January 8th, 2023, using an iodide-based FIGAERO-CIMS (Aerodyne Research Inc., USA) at an urban site in Wuhan (114.6157°E, 30.4577°N). This site is the only provincial supersite operated by local environmental authority for monitoring urban air quality in Wuhan. We obtained valid data of 594 hours, during which meteorological parameters (e.g., relative humidity (RH) and temperature), particulate chemical components (e.g., organic carbon (OC) and sulfate ions (SO_4^{2-})), and gaseous components (e.g., sulfur dioxide (SO_2) and ozone (O_3)) were routinely monitored.

The design of FIGAERO-CIMS for hourly OOMs measurement has been described by previous studies (Zhao et al., 2024; Lopez-Hilfiker et al., 2014; Lee et al., 2014). Briefly, the FIGAERO operated in a measurement cycle of 1 hour alternating between gas-phase and particle-

https://doi.org/10.5194/egusphere-2025-229
Preprint. Discussion started: 17 March 2025

phase modes. During the gas-phase mode, ambient air was drawn at a flow rate of 2 L/min directly into the ion-molecule reactor (IMR), where gaseous molecules were ionized and subsequently detected as adduct ions with the reagent ion I^-. Simultaneously, another flow of ambient air was pulled through a $PM_{2.5}$ cyclone (URG-2000-30EN, URG Corp.) and then a PTFE filter (2 μm Zefluor, 25 mm, Pall Corp.), where particles smaller than 2.5 μm were collected. During the subsequent particle-phase mode, the molecules on the PTFE filter underwent thermal desorption in a heated ultrahigh-purity (UHP) nitrogen flow, which kept at room temperature for 2 minutes, increased to 200 ℃ over 15 minutes, held at 200 ℃ for an additional 15 minutes to ensure the desorption of the majority of OOMs (Lopez-Hilfiker et al., 2014) and then cooled to room temperature within 4 minutes. The desorbed molecules were directed into a turbulent flow IMR. A field blank sample was collected every 24 hours.

2.2 OOMs Identification and Selection

OOMs were identified using a non-target strategy. Mass calibration was performed using ions such as NO_3^-, $C_2F_3O_2^-$, $IC_2H_2O_2^-$, $IC_2F_3HO_2^-$, $IC_3F_5HO_2^-$, and I_3^-, covering a mass range from 62 to 381 m/z. The spectra peaks were iteratively fitted with multiple peaks using a custom peak shape until the residual was reduced to less than 5 % (Lee et al., 2014; Stark et al., 2015). Subsequently, the exact masses of these multiple peaks were matched with the most probable elemental formulas within the ranges of $C_{1\text{-}30}H_{1\text{-}60}O_{0\text{-}20}N_{0\text{-}2}S_{0\text{-}2}X_{0\text{-}2}I_{0\text{-}1}^-$, where X stands for halogen atoms, with mass errors smaller than 10 ppm (mass resolution of ~6000). Isotope distribution was inspected to match with theoretical isotope pattern. Elemental ratio and double bond equivalent (DBE) limits of the formulas were $0.3 \leq H/C \leq 3$, $N/C \leq 0.5$, $O/C \leq 3$, $S/C \leq 1$ and $0 \leq DBE \leq 20$ (Kind and Fiehn, 2007; Lee et al., 2018; Kind and Fiehn, 2006).

Only those OOMs with a unit mass peak area ratio of > 20 % and a sample-to-blank ratio of > 2 were included for further analysis. Thermal desorption may cause OOM decomposition in the particle phase. Using a K-means clustering method, we found that, on average, 25.1% of particle-bound OOM species number and 26.8% of OOM mass detected by the FIGAERO-CIMS could be attributed to thermal decomposition fragments (Supplementary Materials Text S1). These fragments were excluded from the gas/particle partitioning analysis. The overlap of non-fragment particle-

https://doi.org/10.5194/egusphere-2025-229
Preprint. Discussion started: 17 March 2025

bound OOM species with those gas-phase OOM species resulted in 123 species, which were chosen as the target species for subsequent partitioning analysis. Based on our previous work (Figure S1) (Wang et al., 2024), these 123 OOM species were classified to 41 aromatic species (33.7%), 35 monoterpene-derived species (28.3%), 14 isoprene-derived species (11.4%), 11 aliphatic species (8.7%), 10 biomass burning tracers (8.1%), 3 sulfur-containing species (2.4%) and 9 other unknown species (7.3%).

2.3 Observed G/P ratios of OOMs

The concentrations of an OOM species in gas phase and particle phase are calculated as:

$$C_g = \frac{signal_g}{S \times t_g \times Q_g} \times 1000 \qquad (1)$$

$$C_p = \frac{signal_p}{S \times t_p \times Q_p} \times 1000 \qquad (2)$$

where C_g (ng m^{-3}) and C_p (ng m^{-3}) are average concentrations of a species in gas phase and particle phase, respectively, in a measurement interval (e.g., 1 hour in our campaign). $signal_g$ is the integrated signal (unit: counts) of this species during the 21-minute gas-phase measurement time (t_g) in a measurement interval. t_p is the particle sampling time (24 minutes) in a measurement interval. $signal_p$ is the integrated signal of the particle-phase species during thermal desorption period. Q_g and Q_p are the sampling flow rates for the gas phase and particle phase, respectively (Liter min^{-1}). S is the sensitivity of the species (counts per ng). The observed G/P ratio $(\frac{G}{P})_{obs}$ can be calculated as:

$$(\frac{G}{P})_{obs} = \frac{C_g}{C_p} = \frac{signal_g \times t_p \times Q_p}{signal_p \times t_g \times Q_g} \qquad (3)$$

2.4 Comparison with equilibrium G/P ratios

We compared the observed G/P ratios of OOM species in the campaign with those equilibrium G/P ratios $(\frac{G}{P})_{eq}$ estimated from saturated mass concentration C^* and mass concentration of organic aerosol C_{OA} ($C_{OA} = C_{OC} \times 1.4$) using Eq. (4)

$$(\frac{G}{P})_{eq} = \frac{C^*(T)}{C_{OA}} \qquad (4)$$

https://doi.org/10.5194/egusphere-2025-229
Preprint. Discussion started: 17 March 2025

C^* at 300 K of OOMs was calculated using 4 different parameterizations reported by Mohr et al. (2019) , Peräkylä et al. (2020), Ren et al. (2022) and Priestley et al. (2024). Mohr et al. (2019) applied an updated version of the molecular formula parameterization described by Donahue et al. (2011) (based on SIMPOL) to estimate C^* from the numbers of carbon, oxygen, and nitrogen atoms of an OOM species (n_C, n_O, and n_N). This parameterization likely produces C^* of pure compounds. Ren et al. (2022) obtained C^* of OOMs via calibrated C^* *vs.* T_{max} (thermal desorption temperature at which the maximum signal intensity occurs) correlations in thermal desorption process. A similar parameterization formula between C^* and n_C, n_O, and n_N was then derived using multivariate regression. Peräkylä et al. (2020) measured gas and particle-phase concentrations, in an assumed equilibrium state, of α-pinene ozonolysis products using online instruments in a chamber. The C^* of the products were obtained via Eq. (4) and a parameterization was obtained between C^* and n_C, n_O, n_N and the number of hydrogen atoms (n_H). The parameterization of Priestley et al. (2024) was obtained similar to Peräkylä et al. (2020), but the gas and particle-phase concentrations of OOMs were measured in residential wood-burning emissions. The four C^* parameterizations are listed in Text S2. A temperature correction was made based on Eqs. (5) and (6) to convert $C^*(300K)$ to $C^*(T)$ at observed temperatures (Epstein et al., 2010; Li et al., 2024):

$$C^*(T) = C^*(300K) \times \exp\left(\frac{\Delta H_{vap}}{R}\left(\frac{1}{300K} - \frac{1}{T}\right)\right) \quad (5)$$

$$\Delta H_{vap} = -11 \times \log_{10} C^*(300K) + 129 \quad (6)$$

where ΔH_{vap} is the enthalpy of vaporization. R is gas constant. T is the observed temperature in every hour. $C^*(T)$ was then used in Eq. (4) to estimate equilibrium G/P ratios.

2.5 Random forest model

2.5.1 Build random forest models

As illustrated by the scatter plots scatter plots of G/P ratios versus RH or T of example OOM species in Figure S2, no clear correlation is observed between the G/P ratios and environmental variables. More complex interactions and potentially non-linear dependences exist among OOM physicochemical properties, gas and particle phase reactions, and environmental variables. Therefore, we employed random forest models to investigate the influencing factors of the G/P

https://doi.org/10.5194/egusphere-2025-229
Preprint. Discussion started: 17 March 2025

ratios of OOMs.

Our selection of influencing factors (i.e. features) is based on a comprehensive literature review. We categorized 30 features into four groups: (1) 9 molecule features of the OOMs: number of carbon atoms (n_C), number of oxygen atoms (n_O), number of nitrogen atoms (n_N), number of hydrogen atoms (n_H), molecular weight (Mw), double bond equivalent (DBE), hydrogen to carbon atom ratios (H/C), oxygen to carbon atom ratios (O/C) and oxidation state of carbon (OSc). (2) 7 meteorological features: RH, temperature (T), wind speed (WS), wind direction (represented by sine and cosine functions to preserve the periodicity, denoted as WD_sin and WD_cos), ultraviolet-A (UV-A), ultraviolet-B (UV-B), photolysis rates of HONO (PR_{HONO}). (3) 4 gaseous composition features: SO_2, O_3, nitrogen dioxide (NO_2) and ammonia (NH_3). (4) 10 particle composition features: OC, elemental carbon (EC), SO_4^{2-}, nitrate ions (NO_3^-), chloride ions (Cl^-), ammonium ions (NH_4^+), fine particulate matter ($PM_{2.5}$), potassium ions (K^+), as well as aerosol-phase pH and liquid water content (LWC). Calculation details of pH and LWC using ISORROPIA-II model (Fountoukis and Nenes, 2007) are provided in Text S3. This feature selection scheme guarantees a balanced representation of pertinent factors, while preserving the simplicity and predictive efficacy of the models.

First, we developed a multi-species model involving 123 OOM species to predict the $(\frac{G}{P})_{obs}$ of OOMs from molecule features, meteorological features, gas and particle composition features. A total of 73062 $(\frac{G}{P})_{obs}$ values for 123 species with hourly resolution were collected in the winter campaign. Outlier removal is described in Text S4. The data used for modeling were divided into training data used for model training and test data used for model evaluation, which comprise 85% and 15% of the total data, respectively.

Second, we selected six typical OOMs, including more volatile ($C_5H_8O_4$, $C_6H_{10}O_4$, $C_6H_5NO_3$, $C_7H_7NO_3$, C^* range: $10^{3.90}$~$10^{6.53}$ μg m^{-3}) and less volatile species ($C_{10}H_{16}O_4$, $C_{12}H_{21}NO_9$, C^* range: $10^{-4.73}$ ~$10^{1.18}$ μg m^{-3}) according to the C^* parameterization of Mohr et al. (2019). $C_5H_8O_4$ (glutaric acid (Lee et al., 2014; Reyes-Villegas et al., 2018)) and $C_6H_{10}O_4$ (adipic acid (Ye et al., 2021; Lee et al., 2014)) are small dicarboxylic acids ($C \leqslant 6$) typically formed through photochemical degradation of reactions of alkenes, aldehydes, longer-chain acids (Kawamura and Sakaguchi, 1999)

https://doi.org/10.5194/egusphere-2025-229
Preprint. Discussion started: 17 March 2025

or other low-oxygen organic compounds (Grosjean and Friedlander, 1980) in urban atmosphere (Kawamura and Ikushima, 1993). $C_6H_5NO_3$ (Huang et al., 2019; Cai et al., 2022) and $C_7H_7NO_3$ (Huang et al., 2019; Cai et al., 2022) are nitrophenols either directly emitted from vehicle exhaust (Tremp et al., 1993), coal and wood combustion (Huang et al., 2019), industrial processes (Harrison et al., 2005) or being formed through the nitration of phenol in gas or liquid phase (Lüttke and Levsen, 1997). $C_{10}H_{16}O_4$ is primarily derived the oxidation of monoterpenes (Ye et al., 2019; Barreira et al., 2021). $C_{12}H_{21}NO_9$ is an organic nitrate from long-chain alkane oxidation under high-NO_x conditions (Wang and Ruiz, 2018).

Third, single-species models were tailored to predict the gas/particle partitioning behaviors of these six individual OOMs under varying meteorological and gas-particle composition conditions. We also build random forest models to investigate how $(\frac{G}{P})_{obs}$ of the six OOMs deviate from $(\frac{G}{P})_{eq}$ under varying meteorological and gas/particle composition conditions.

2.5.2 Model optimization, evaluation and feature importance analysis

To optimize and evaluate the model's performance, we applied a combination of Grid Search and Cross-Validation methods. First, we employed Grid Search to tune the hyperparameters of the Random Forest model. The search space included the following hyperparameters: n_estimators (the number of decision trees), max_depth (the maximum depth of each tree), and max_features (the number of features considered for splitting at each node) and min_samples_split (the minimum number of samples required to split an internal node). For each combination of hyperparameters, we used 5-fold Cross-Validation on the training set with coefficient of determination (R^2) as the primary metric to assess model performance and identify the best configuration.

After selecting the optimal hyperparameters, we further evaluated the final model using 5-fold Cross-Validation to assess its performance. In this evaluation, both R^2 and Root Mean Square Error (RMSE) were used as metrics: R^2 indicates the proportion of variance in the G/P ratio explained by the model. RMSE, on the other hand, quantifies the average prediction error and is calculated as the square root of the average squared differences between the predicted and actual values. The final model performance was determined by averaging the R^2 and RMSE values across the 5 validation

https://doi.org/10.5194/egusphere-2025-229
Preprint. Discussion started: 17 March 2025

sets. All model tuning and evaluation were conducted using Python (v.3.8).

To quantify the influence of each feature on the G/P ratio, we computed SHAP (SHapley Additive exPlanations) value of each feature for each sample (i.e., at each hour) using the SHAP package (v.0.40.0) in Python (v.3.8). A positive SHAP value indicates that the feature contributes positively to the G/P ratio, while a negative SHAP value means it has a negative contribution. The SHAP values were then fitted with a generalized additive model (GAM) using the pygam package (v.0.8.0) to further identify the sensitive ranges where the changes of feature values significantly affect the SHAP values. For more details, please refer to Text S5. We utilized two-way Partial Dependence Plots (PDPs) (Chen et al., 2024; Shi et al., 2023; Zhang et al., 2022) to analyze the joint effects of T and RH on the predicted G/P ratio. This analysis yielded a comprehensive understanding of how simultaneous changes of T and RH affect the observed G/P ratio, thereby unveiling the complex dynamics among these variables. For more details, please refer to the Text S6.

3. Results and Discussion

3.1 Observed G/P ratios of OOMs and comparison with equilibrium partitioning

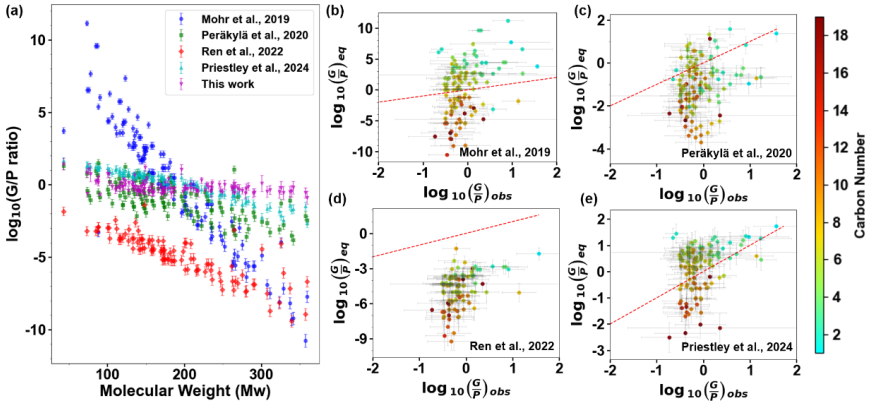

Figure 1. Comparison of $(\frac{G}{P})_{obs}$ of 123 OOMs with corresponding $(\frac{G}{P})_{eq}$ predicted by Eq. (4). C^* was estimated from the parameterizations of Mohr et al. (2019), Peräkylä et al. (2020), Ren et al. (2022) and Priestley et al. (2024), respectively. Error bars of $(\frac{G}{P})_{obs}$ denote the range of G/P ratios

https://doi.org/10.5194/egusphere-2025-229
Preprint. Discussion started: 17 March 2025

observed under varying conditions for 594 samples (i.e. 594 hours). Error bars of $(\frac{G}{P})_{eq}$ denote the variations with temperature and C_{OA}. Color scales in (b-e) denote carbon number of OOM species. Dashed red lines in (b-e) denote a 1:1 correspondence.

As shown in Figure 1a, although G/P ratios generally decrease with increasing molecular weight, the observed G/P ratios $(\frac{G}{P})_{obs}$ show a narrower range (10^{-1}~$10^{1.5}$) than the equilibrium G/P ratios $(\frac{G}{P})_{eq}$ predicted from Eq. (4). The differences could be up to 10 orders of magnitude, depending on C^* parameterization. The $(\frac{G}{P})_{eq}$ predicted by Mohr et al. (2019) are higher than $(\frac{G}{P})_{obs}$ for the OOMs with n_C = 2-5 and lower than $(\frac{G}{P})_{obs}$ for the OOMs with n_C > 8 (Figure 1b). On the basis of thermal desorption temperature, Ren et al. (2022) predicts lower equilibrium G/P ratios than all other parameterizations and our observation. Although Peräkylä et al. (2020) also predicted lower G/P ratios, their ratios are much closer to our observation than Ren et al. (2022). Among all the predictions, the prediction from Priestley et al. (2024) is most close to our observation. This is because their C^* parameterization is based on the measured gas and particle-phase concentrations of OOMs in fresh or aged residential wood-burning emissions. Their predicted G/P ratio is thus inherently consistent with the observed G/P ratios in our study.

In theory, no matter which C^* parameterization is used in Eq. (4), the temporal variation of $(\frac{G}{P})_{eq}$ for an OOM species depends solely on C_{OA} and temperature. Therefore, we are able to obtain a normalized $(\frac{G}{P})_{eq}$, which is independent of C^* parameterization, by dividing the $(\frac{G}{P})_{eq}$ of an OOM by its maximum value. Diurnal variations of normalized $(\frac{G}{P})_{eq}$ of $C_5H_8O_4$ and $C_7H_7NO_3$ are shown in Figure 2a-2b and those of other four selected OOMs are shown in Figure S3. We found similar diurnal variations for all six OOMs: a peak G/P ratio appeared in the afternoon, which is attributed to higher temperature. In contrast, we observed significant fluctuations of $(\frac{G}{P})_{obs}$ diurnal variations for the six OOM species during the campaign, as shown in Figure 2c-2h. This indicates that the extent of deviation of actual gas/particle partitioning from equilibrium state fluctuates over time, driven by other unknown factors. In this study, we will first examine the influencing factors

https://doi.org/10.5194/egusphere-2025-229
Preprint. Discussion started: 17 March 2025

of gas-particle distribution of OOMs in urban atmosphere during the winter campaign (Section 3.2), followed by an investigation into the factors contributing to the discrepancies between observed and equilibrium G/P ratios (Section 3.3).

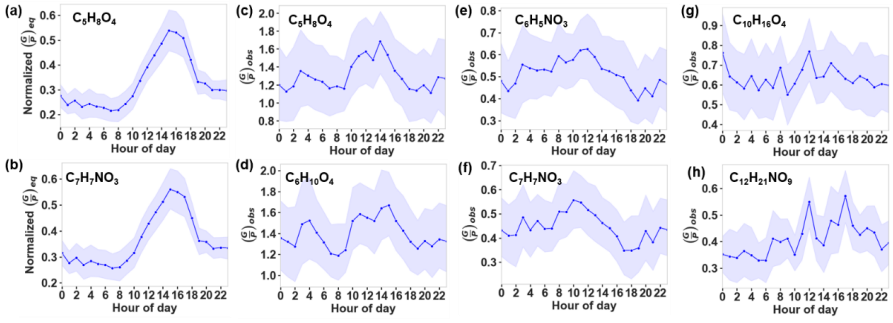

Figure 2. Diurnal variations of (a-b) Normalized equilibrium G/P ratios for the selected species ($C_5H_8O_4$ and $C_7H_7NO_3$) and (c-h) observed G/P ratios during the campaign. Solid line denotes the average value and filled area denotes the 95% confidence intervals of the mean.

3.2 Influencing Factors of the observed G/P ratios of OOMs

3.2.1 Multi-species model performance and key features

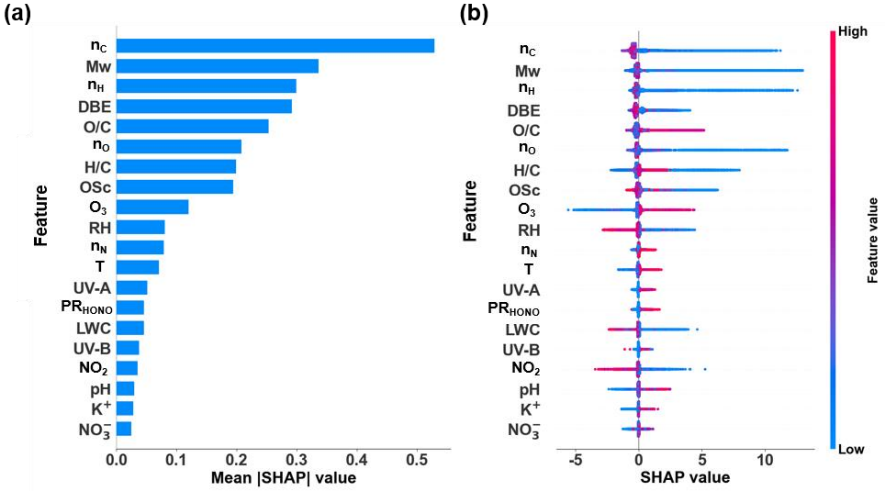

Figure 3. Multi-Species Model: (a) Feature importance based on the mean of absolute SHAP values

https://doi.org/10.5194/egusphere-2025-229
Preprint. Discussion started: 17 March 2025

calculated for 594 samples (i.e. 594 hours) to predict the G/P ratio. (b) Distribution of SHAP values in 594 samples for top 20 features.

The 5-fold cross-validation demonstrates that a predictive multi-species model with satisfactory performance was developed, with R^2=0.88 ± 0.02 and RMSE = 1.76 ± 0.13 (Figure S4). Mean absolute SHAP values indicate the average importance of each feature in predicting the observed G/P ratios (Figure 3a). The model highlights that intrinsic molecule features, such as n_C, Mw, n_H, DBE, far outweigh meteorological and chemical composition features in the model's predictions. Of the nine molecular features, eight are ranked as highly important, with n_N being comparatively less influential.

Figure 3b shows the SHAP value distribution for each feature. For molecule features, such as n_C, Mw, n_H and n_O, high feature values are associated with negative SHAP, while low feature values are associated with positive SHAP. This suggests that large molecules with high n_C, Mw, n_H and n_O, and consequently lower volatility, are more likely to partition into the particle phase, thereby reducing the G/P ratio.

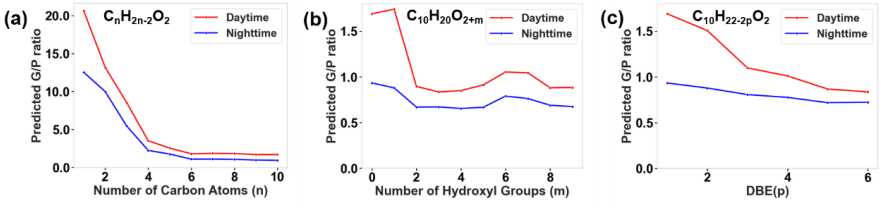

Figure 4. Predicted G/P ratios using the developed multi-species model for (a) Monocarboxylic acids as a function of the number of carbon atoms, (b) Modified 10-carbon monocarboxylic acids as a function of the number of additional hydroxyl groups and (c) Modified 10-carbon monocarboxylic acids as a function of DBE, under average daytime and nighttime environmental and gas/particle composition conditions.

However, the molecule features about oxidation state and unsaturation degree did not show consistent effects on the observed G/P ratios. For example, OSc has a negative effect on the G/P ratios, whereas O/C has a positive effect. DBE has a negative effect on the G/P ratios, whereas H/C shows a mixed positive or negative effect. This is due to the fact that these features are dependent

https://doi.org/10.5194/egusphere-2025-229
Preprint. Discussion started: 17 March 2025

variables as a function of n_C, n_H, n_N and n_O. To isolate the effect of oxidation and unsaturation-related features, we utilized the trained random forest model to predict G/P ratios of modified C_{10} monocarboxylic acid with varying number of hydroxyl group and DBE (Figure 4b and 4c). Other features in the model were fixed at average daytime or nighttime values observed during the campaign (see Table S1, S2). For comparison, the isolated effect of carbon atom number is also plotted (Figure 4a).

Figure 4 demonstrates that the number of carbon atoms exerts the most significant influence on the predicted G/P ratio, which decreases sharply as the carbon atom number increases from 1 to 4. Beyond this point, the ratio levels off. For modified 10-carbon monocarboxylic acids, G/P ratios are high when there is one or no hydroxyl group (Figure 4b). The G/P ratio levels off when the number of hydroxyl group exceeds 2. The G/P ratio decreases with increasing DBE value (Figure 4c). When DBE value exceeds 5, the G/P ratio change becomes minimal. In all the subplots, the G/P ratio during nighttime is consistently lower than that during daytime, which could be attributed to enhanced partitioning from gas to particles at lower nighttime temperature.

3.2.2 Identification of key features and sensitive analysis in single-species models

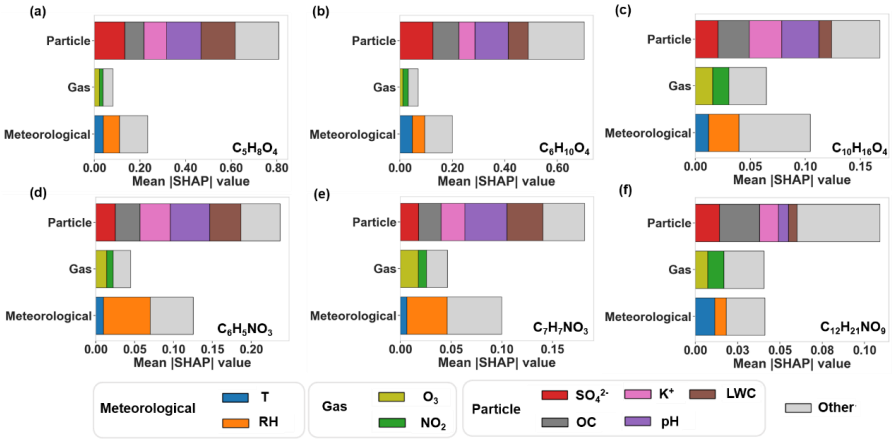

Figure 5. SHAP value analysis of three categories of features. Mean |SHAP| denotes the mean absolute SHAP values calculated for 594 samples (i.e. 594 hours): (a) glutaric acid ($C_5H_8O_4$), (b) adipic acid ($C_6H_{10}O_4$), (c) monoterpene oxidation products ($C_{10}H_{16}O_4$), (d, e) nitrophenol ($C_6H_5NO_3$

https://doi.org/10.5194/egusphere-2025-229
Preprint. Discussion started: 17 March 2025

and $C_7H_7NO_3$), and (f) nitrated aliphatic acid ($C_{12}H_{21}NO_9$).

By excluding molecule features, single-species models focus on the prediction of observed gas/particle partitioning behaviors of individual OOMs from meteorological and gas/particle composition features. The evaluation results and optimal parameters of the six single-species models are presented in Table S3. All models show acceptable performance (R^2 = 0.51-0.88). For all six OOMs, particle composition features dominate over meteorological and gaseous composition features in predicting the G/P ratios (Figure 5). Particle composition features LWC, OC, K^+, SO_4^{2-} and pH, as well as RH, consistently play important roles in influencing the G/P ratios of these species. Below, we (1) examined the positive or negative effects of these features one by one (Figure 6a), and (2) identified the sensitive ranges of these features by fitting SHAP values against feature values using a GAM (Figure 7).

pH is among the two most influential factors for the gas/particle partitioning of five species ($C_5H_8O_4$, $C_6H_{10}O_4$, $C_6H_5NO_3$, $C_7H_7NO_3$ and $C_{10}H_{16}O_4$) with a sensitive range of 3.5–4.5 (as illustrated for $C_6H_{10}O_4$ in Figure 7a). Within this range, an increase in pH results in a pronounced decrease of the G/P ratio. This phenomenon can be attributed to the enhanced partitioning of OOMs with acidic functional groups from gas to particles with elevated pH (Su et al., 2020).

RH has a positive effect, ranking among the top 5 significant features, on the G/P ratios of three OOMs $C_6H_5NO_3$, $C_7H_7NO_3$, and $C_{10}H_{16}O_4$ (Figure 6a). SHAP value is sensitive to RH across the full RH range (20%-80%, illustrated by an example $C_6H_5NO_3$ in Figure 7b). LWC also has a significant positive effect for $C_5H_8O_4$, $C_6H_{10}O_4$, $C_6H_5NO_3$, and $C_7H_7NO_3$. For example, in the case of $C_5H_8O_4$, a sharp increase in the G/P ratio is observed within the LWC range below 20 μg m^{-3} (Figure 7c). The underlying mechanism of this behavior is unclear. One explanation is that the increase of RH and LWC in particles may facilitate hydrolysis reactions of organic compounds, thereby reducing the concentration of these OOMs in particle phase. It is also possible that the thermal desorption and subsequent detection of particle-bound OOMs were prohibited in aerosol particles with more moisture.

Temperature ranged from -1.6 °C to 14.9 °C during the winter campaign. Although temperature increase tends to elevate the G/P ratios (Figure 6a), the models show that temperature did not rank

https://doi.org/10.5194/egusphere-2025-229
Preprint. Discussion started: 17 March 2025

as important feature for 5 out of the 6 OOM species. We evaluated the effect of temperature on G/P ratios using two-way partial dependence plots (Figure S5). G/P ratio is sensitive to temperature change only for two dicarboxylic acids ($C_5H_8O_4$ and $C_6H_{10}O_4$, Figure S5a-S5b) and for $C_{12}H_{21}NO_9$ in a narrow temperature range of 10-13 °C (Figure S5f and Figure 7d). The G/P ratios of $C_6H_5NO_3$, $C_7H_7NO_3$ and $C_{10}H_{16}O_4$ are not sensitive to temperature across most of the RH range. This behavior may be attributed to other factors that hinder the rapid equilibrium partitioning of OOMs when temperature changes.

https://doi.org/10.5194/egusphere-2025-229
Preprint. Discussion started: 17 March 2025

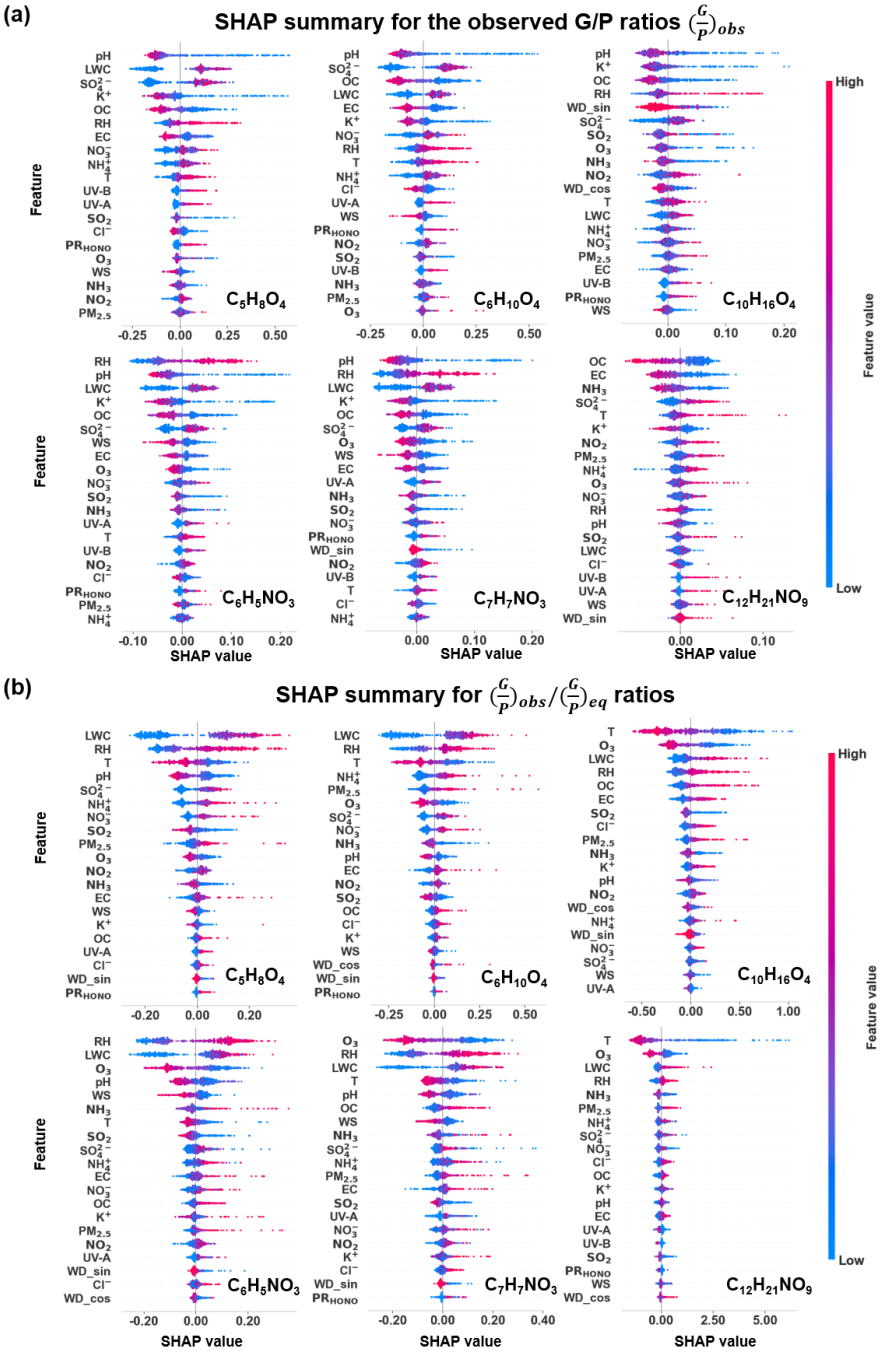

349

350 **Figure 6**. SHAP summary plots for feature importance based on the random forest model for glutaric

https://doi.org/10.5194/egusphere-2025-229
Preprint. Discussion started: 17 March 2025

acid ($C_5H_8O_4$), adipic acid ($C_6H_{10}O_4$), monoterpene oxidation product ($C_{10}H_{16}O_4$), nitrophenol ($C_6H_5NO_3$ and $C_7H_7NO_3$), and nitrated aliphatic acid ($C_{12}H_{21}NO_9$). Features are prioritized in descending order based on their importance. (a) SHAP summary for the observed G/P ratios $(\frac{G}{P})_{obs}$. (b) SHAP summary for $(\frac{G}{P})_{obs}/(\frac{G}{P})_{eq}$ ratios.

OC has a significant negative impact (i.e., rank among the top 5) on the G/P ratios of all six species, being consistent with Eq. (4), where the equilibrium G/P ratios are inversely proportional to C_{OA}. Taking $C_{12}H_{21}NO_9$ as example (Figure 7e), the SHAP values decrease monotonically with C_{OA} in the entire C_{OA} range (5-25 μg m^{-3}). For this compound, EC ranks as the second most influential factor, exerting a notable negative impact below 4 μg m^{-3} (Figure 7f).

SO_4^{2-} has a positive effect (i.e., rank among the top 5) on the G/P ratios of $C_5H_8O_4$, $C_6H_{10}O_4$ and $C_{12}H_{21}NO_9$. For example, in the case of $C_6H_{10}O_4$, the G/P ratio rises rapidly with increasing SO_4^{2-} concentrations below 6 μg m^{-3} (Figure 7g). This may be partly related to the fact that SO_4^{2-} is a highly hydrophilic component (Thaunay et al., 2015), which makes its effect similar to that of LWC. In addition, an increase of sulfate in aerosols is often associated with enhanced acidity and a decrease in pH (Zhang et al., 2007), which drives OOM from particle to gas phase as we explained above.

K^+ has a negative effect on the G/P ratios of $C_5H_8O_4$, $C_{10}H_{16}O_4$, $C_6H_5NO_3$ and $C_7H_7NO_3$. Taking $C_{10}H_{16}O_4$ as example, the G/P ratio decreases rapidly with K^+ in the concentration range of below 1 μg m^{-3} (Figure 7h). K^+ is considered as a tracer of biomass burning. The increase of K^+ is generally associated with higher pollution levels and higher OC concentrations. The effect of K^+ on the G/P ratio is thus similar to that of OC.

https://doi.org/10.5194/egusphere-2025-229
Preprint. Discussion started: 17 March 2025

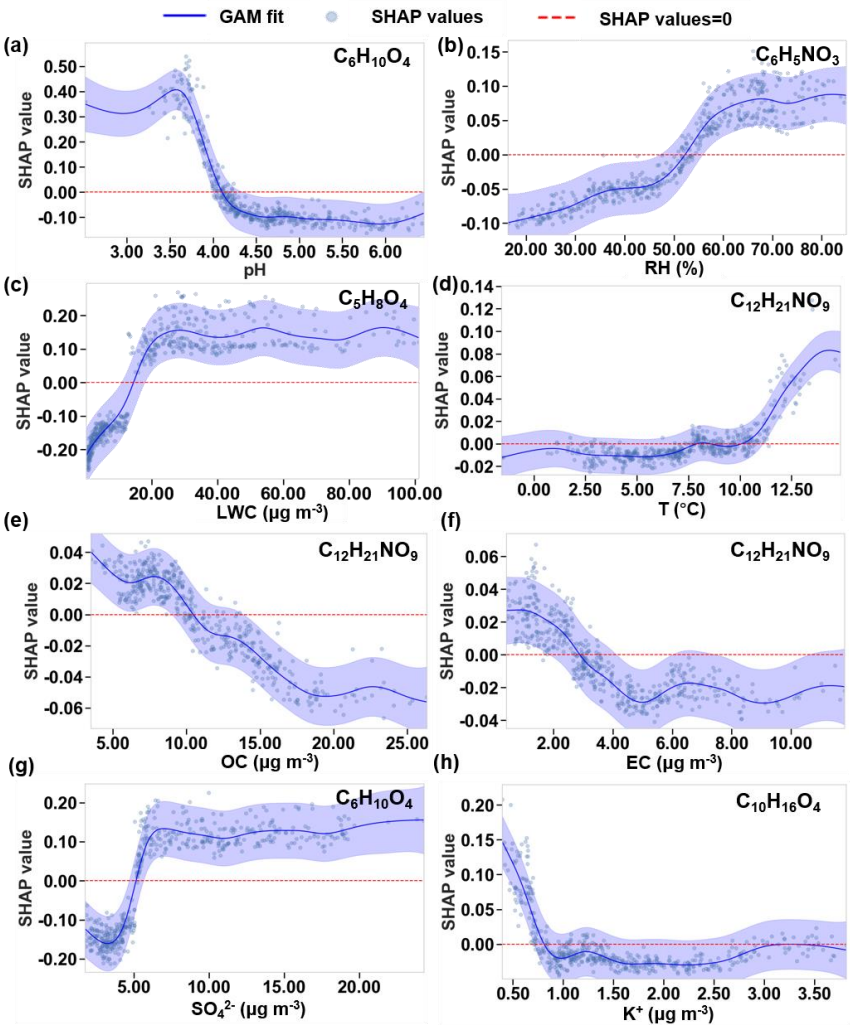

Figure 7. Curve fitting of SHAP values versus features using a GAM, illustrating the sensitive ranges where the changes of feature values significantly affect the SHAP values. Only the most affected OOM species by the eight features are shown. (a) RH for $C_6H_5NO_3$. (b) LWC for $C_5H_8O_4$. (c) pH for $C_6H_{10}O_4$. (d) Temperature for $C_{12}H_{21}NO_9$. (e) OC for $C_{12}H_{21}NO_9$. (f) EC for $C_{12}H_{21}NO_9$. (g) $SO4^{2-}$ for $C_6H_{10}O_4$. (h) K^+ for $C_{10}H_{16}O_4$. Blue line denotes the GAM fit. Shaded area indicates 95% confidence interval. Dots are the SHAP values for 594 samples (i.e. 594 hours). Red dashed line denotes SHAP value of 0.

https://doi.org/10.5194/egusphere-2025-229
Preprint. Discussion started: 17 March 2025

3.3 Identifying key factors driving the deviations of gas/particle partitioning from equilibrium state

To investigate the deviations of observed gas/particle partitioning from equilibrium state, we first calculate the ratios of $(\frac{G}{P})_{obs}$ over normalized $(\frac{G}{P})_{eq}$ in every hour for the selected six OOM species. Normalized $(\frac{G}{P})_{eq}$ was used here in order to offset the effect of the C^* parameterization selection. We then developed new random forest models to investigate the effects of meteorological and gas/particle composition features on the $(\frac{G}{P})_{obs}/(\frac{G}{P})_{eq}$ ratios. All the models show acceptable performance (R^2 = 0.52-0.83) (Table S4).

Figure 6b presents the SHAP analysis results for the $(\frac{G}{P})_{obs}/(\frac{G}{P})_{eq}$ ratios of the six OOMs. The models identify RH, LWC, O_3 and temperature as four influential factors driving the deviations from equilibrium partitioning. Positive correlations are observed between the SHAP values of $(\frac{G}{P})_{obs}/(\frac{G}{P})_{eq}$ and RH and LWC for all six compounds. This indicates that RH and LWC have stronger positive effect on $(\frac{G}{P})_{obs}$ than their effect on $(\frac{G}{P})_{eq}$, which should be negligible according to Eq. (4). Temperature is shown to be a negative factor driving the deviation from equilibrium partitioning, suggesting that temperature has a stronger influence on $(\frac{G}{P})_{eq}$ than $(\frac{G}{P})_{obs}$. This is consistent with our earlier result that $(\frac{G}{P})_{obs}$ is not sensitive to temperature. Surprisingly, O_3 is identified as an important influential factor with negative effect, particularly for the three nitrophenols and monoterpene oxidation product $C_{10}H_{16}O_4$. Since O_3 is not expected to change $(\frac{G}{P})_{eq}$, the negative impact of O_3 on $(\frac{G}{P})_{obs}/(\frac{G}{P})_{eq}$ ratio could be explained by the fact that high O_3 is likely to deplete gas phase OOMs, thereby reducing $(\frac{G}{P})_{obs}$.

Conclusions

We measured the G/P ratios of OOM species using a FIGAERO-CIMS in urban atmosphere in a winter campaign. The observed G/P ratios show a narrower range than the equilibrium G/P ratios predicted from C^* and C_{OA}. The difference between observed and equilibrium G/P ratios could be

https://doi.org/10.5194/egusphere-2025-229
Preprint. Discussion started: 17 March 2025

up to 10 orders of magnitude, depending on C^* parameterization. Our observed G/P ratio is inherently closer to the equilibrium G/P ratios predicted from the C^* parameterization by Priestley et al., which was derived from measured G/P ratios in wood-burning emissions. Our random forest models identified RH, LWC, O_3 and temperature as four influential factors driving the deviations of gas/particle partitioning from equilibrium state.

Random forest models with satisfactory performance were developed to predict observed G/P ratios. Intrinsic molecule features, such as n_C, Mw, n_H, DBE, far outweigh meteorological and chemical composition features in the model's predictions. Large molecules with high n_C, Mw, n_H and n_O, and consequently lower volatility, are more likely to partition into the particle phase, thereby reducing the G/P ratio. As dependent variables, oxidation state and unsaturation do not show consistently positive or negative effects on the observed G/P ratios. If other variables are fixed, the model predicts that G/P ratios generally decrease with the addition of oxygen atom and DBE.

Particle composition features dominate over meteorological and gaseous composition features in predicting the G/P ratio of a given OOM species. Among those particle features, pH, RH, LWC, OC, K^+ and SO_4^{2-} consistently play important roles in influencing the G/P ratios of the six selected OOM species, showing either positive or negative effect. We also identified the sensitive ranges where the changes of these features significantly affect the SHAP values and provided valuable insights for future research in atmospheric chemistry. It is surprising that temperature does not emerge as an important factor influencing the G/P ratios for five out of the six selected OOM species. Our model suggests that other factors, most likely associated with the particle composition, inhibit the gas/particle partitioning of OOMs in response to temperature change.

The random forest models developed in this study have certain limitations. Aerosol particle coating may serve as an inhibitory factor of gas/particle partitioning. However, the mixing state and morphology of aerosol particles were not considered in the model due to the challenges in quantifying these features with high resolution. Furthermore, the model was based solely on the data collected during the winter season and for specific groups of OOM species present in urban atmosphere. To enhance the robustness of the gas-to-particle partitioning model, additional data collected under a broader range of atmospheric conditions are necessary.

https://doi.org/10.5194/egusphere-2025-229
Preprint. Discussion started: 17 March 2025

Data availability

All data in this study are available from corresponding author upon request.

Author contributions

HY designed the experiment. XW, BZ and NC contributed to data collection. XW and HY analyzed the data and wrote the manuscript.

Competing interests

The contact author has declared that none of the authors has any competing interests.

Financial support

This research was supported by the National Natural Science Foundation of China (42175131) and the Fundamental Research Funds (No. G1323523063) for the Central Universities, China University of Geosciences (Wuhan).

References

Barreira, L. M. F., Ylisirnio, A., Pullinen, I., Buchholz, A., Li, Z. J., Lipp, H., Junninen, H., Horrak, U., Noe, S. M., Krasnova, A., Krasnov, D., Kask, K., Talts, E., Niinemets, U., Ruiz-Jimenez, J., and Schobesberger, S.: The importance of sesquiterpene oxidation products for secondary organic aerosol formation in a springtime hemiboreal forest, Atmos. Chem. Phys., 21, 11781-11800, https://doi.org/10.5194/acp-21-11781-2021, 2021.

Bland, G. D., Battifarano, M., Pradas del Real, A. E., Sarret, G., and Lowry, G. V.: Distinguishing Engineered TiO2 Nanomaterials from Natural Ti Nanomaterials in Soil Using spICP-TOFMS and Machine Learning, Environ. Sci. Technol., 56, 2990-3001, https://doi.org/10.1021/acs.est.1c02950, 2022.

Boiko, D. A., Kozlov, K. S., Burykina, J. V., Ilyushenkova, V. V., and Ananikov, V. P.: Fully Automated Unconstrained Analysis of High-Resolution Mass Spectrometry Data with Machine Learning, J. Am. Chem. Soc., 144, 14590-14606, https://doi.org/10.1021/jacs.2c03631, 2022.

Cai, J., Wu, C., Wang, J., Du, W., Zheng, F., Hakala, S., Fan, X., Chu, B., Yao, L., Feng, Z., Liu, Y., Sun, Y., Zheng, J., Yan, C., Bianchi, F., Kulmala, M., Mohr, C., and Daellenbach, K. R.: Influence of organic aerosol molecular composition on particle absorptive properties in autumn Beijing, Atmos. Chem. Phys., 22, 1251-1269, https://doi.org/10.5194/acp-22-1251-2022, 2022.

Chen, Q., Shao, K., and Zhang, S.: Enhanced PM2.5 estimation across China: An AOD-independent two-

https://doi.org/10.5194/egusphere-2025-229
Preprint. Discussion started: 17 March 2025

stage approach incorporating improved spatiotemporal heterogeneity representations, J. Environ. Manage., 368, 122107, https://doi.org/10.1016/j.jenvman.2024.122107, 2024.

Christopoulos, C. D., Garimella, S., Zawadowicz, M. A., Möhler, O., and Cziczo, D. J.: A machine learning approach to aerosol classification for single-particle mass spectrometry, Atmos. Meas. Tech., 11, 5687-5699, https://doi.org/10.5194/amt-11-5687-2018, 2018.

Donahue, N. M., Epstein, S. A., Pandis, S. N., and Robinson, A. L.: A two-dimensional volatility basis set: 1. organic-aerosol mixing thermodynamics, Atmos. Chem. Phys., 11, 3303-3318, https://doi.org/10.5194/acp-11-3303-2011, 2011.

Epstein, S. A., Riipinen, I., and Donahue, N. M.: A Semiempirical Correlation between Enthalpy of Vaporization and Saturation Concentration for Organic Aerosol, Environ. Sci. Technol., 44, 743-748, https://doi.org/10.1021/es902497z, 2010.

Fountoukis, C. and Nenes, A.: ISORROPIA II: a computationally efficient thermodynamic equilibrium model for K^+–Ca^{2+}–Mg^{2+}–NH_4^+–Na^+–SO_4^{2-}–NO_3^-–Cl^-–H_2O aerosols, Atmos. Chem. Phys., 7, 4639-4659, https://doi.org/10.5194/acp-7-4639-2007, 2007.

Fowler, K., Connolly, P. J., Topping, D. O., and O'Meara, S.: Maxwell–Stefan diffusion: a framework for predicting condensed phase diffusion and phase separation in atmospheric aerosol, Atmos. Chem. Phys., 18, 1629-1642, https://doi.org/10.5194/acp-18-1629-2018, 2018.

Franklin, E. B., Yee, L. D., Aumont, B., Weber, R. J., Grigas, P., and Goldstein, A. H.: Ch3MS-RF: a random forest model for chemical characterization and improved quantification of unidentified atmospheric organics detected by chromatography–mass spectrometry techniques, Atmos. Meas. Tech., 15, 3779-3803, https://doi.org/10.5194/amt-15-3779-2022, 2022.

George, I. J., Vlasenko, A., Slowik, J. G., Broekhuizen, K., and Abbatt, J. P. D.: Heterogeneous oxidation of saturated organic aerosols by hydroxyl radicals: uptake kinetics, condensed-phase products, and particle size change, Atmos. Chem. Phys., 7, 4187-4201, https://doi.org/10.5194/acp-7-4187-2007, 2007.

Gong, X., Wex, H., Müller, T., Henning, S., Voigtländer, J., Wiedensohler, A., and Stratmann, F.: Understanding aerosol microphysical properties from 10 years of data collected at Cabo Verde based on an unsupervised machine learning classification, Atmos. Chem. Phys., 22, 5175-5194, https://doi.org/10.5194/acp-22-5175-2022, 2022.

Grosjean, D. and Friedlander, S.: Formation of organic aerosols from cyclic olefins and diolefins, Adv. Environ. Sci. Technol.;(United States), 9, 1980.

Harrison, M. A. J., Barra, S., Borghesi, D., Vione, D., Arsene, C., and Iulian Olariu, R.: Nitrated phenols in the atmosphere: a review, Atmos. Environ., 39, 231-248, https://doi.org/10.1016/j.atmosenv.2004.09.044, 2005.

Hildebrandt, L., Donahue, N. M., and Pandis, S. N.: High formation of secondary organic aerosol from the photo-oxidation of toluene, Atmos. Chem. Phys., 9, 2973-2986, https://doi.org/10.5194/acp-9-2973-2009, 2009.

Huang, W., Saathoff, H., Shen, X., Ramisetty, R., Leisner, T., and Mohr, C.: Seasonal characteristics of

https://doi.org/10.5194/egusphere-2025-229
Preprint. Discussion started: 17 March 2025

organic aerosol chemical composition and volatility in Stuttgart, Germany, Atmos. Chem. Phys., 19, 11687-11700, https://doi.org/10.5194/acp-19-11687-2019, 2019.

Jang, M., Czoschke, N. M., Lee, S., and Kamens, R. M.: Heterogeneous Atmospheric Aerosol Production by Acid-Catalyzed Particle-Phase Reactions, Science, 298, 814-817, https://doi.org/10.1126/science.1075798, 2002.

Kawamura, K. and Ikushima, K.: Seasonal changes in the distribution of dicarboxylic acids in the urban atmosphere, Environ. Sci. Technol., 27, 2227-2235, 1993.

Kawamura, K. and Sakaguchi, F.: Molecular distributions of water soluble dicarboxylic acids in marine aerosols over the Pacific Ocean including tropics, J. Geophys. Res. Atmos., 104, 3501-3509, https://doi.org/10.1029/1998JD100041, 1999.

Kind, T. and Fiehn, O.: Metabolomic database annotations via query of elemental compositions: Mass accuracy is insufficient even at less than 1 ppm, BMC Bioinformatics, 7, 234, https://doi.org/10.1186/1471-2105-7-234, 2006.

Kind, T. and Fiehn, O.: Seven Golden Rules for heuristic filtering of molecular formulas obtained by accurate mass spectrometry, BMC Bioinformatics, 8, 105, https://doi.org/10.1186/1471-2105-8-105, 2007.

Lee, B. H., Lopez-Hilfiker, F. D., Mohr, C., Kurten, T., Worsnop, D. R., and Thornton, J. A.: An Iodide-Adduct High-Resolution Time-of-Flight Chemical-Ionization Mass Spectrometer: Application to Atmospheric Inorganic and Organic Compounds, Environ. Sci. Technol., 48, 6309-6317, https://doi.org/10.1021/es500362a, 2014.

Lee, B. H., Lopez-Hilfiker, F. D., D'Ambro, E. L., Zhou, P., Boy, M., Petäjä, T., Hao, L., Virtanen, A., and Thornton, J. A.: Semi-volatile and highly oxygenated gaseous and particulate organic compounds observed above a boreal forest canopy, Atmos. Chem. Phys., 18, 11547-11562, https://doi.org/10.5194/acp-18-11547-2018, 2018.

Li, L., Thomsen, D., Wu, C., Priestley, M., Iversen, E. M., Tygesen Skonager, J., Luo, Y., Ehn, M., Roldin, P., Pedersen, H. B., Bilde, M., Glasius, M., and Hallquist, M.: Gas-to-Particle Partitioning of Products from Ozonolysis of Δ3-Carene and the Effect of Temperature and Relative Humidity, J. Phys. Chem. A, 128, 918-928, https://doi.org/10.1021/acs.jpca.3c07316, 2024.

Lin, G.-Y., Chen, H.-W., Chen, B.-J., and Chen, S.-C.: A machine learning model for predicting PM2.5 and nitrate concentrations based on long-term water-soluble inorganic salts datasets at a road site station, Chemosphere, 289, 133123, https://doi.org/10.1016/j.chemosphere.2021.133123, 2022.

Liu, X., Day, D. A., Krechmer, J. E., Brown, W., Peng, Z., Ziemann, P. J., and Jimenez, J. L.: Direct measurements of semi-volatile organic compound dynamics show near-unity mass accommodation coefficients for diverse aerosols, Commun. Chem., 2, 98, https://doi.org/10.1038/s42004-019-0200-x, 2019.

Lopez-Hilfiker, F. D., Mohr, C., Ehn, M., Rubach, F., Kleist, E., Wildt, J., Mentel, T. F., Lutz, A., Hallquist, M., Worsnop, D., and Thornton, J. A.: A novel method for online analysis of gas and particle composition: description and evaluation of a Filter Inlet for Gases and AEROsols (FIGAERO), Atmos.

https://doi.org/10.5194/egusphere-2025-229
Preprint. Discussion started: 17 March 2025

Meas. Tech., 7, 983-1001, https://doi.org/10.5194/amt-7-983-2014, 2014.

Lüttke, J. and Levsen, K.: Phase partitioning of phenol and nitrophenols in clouds, Atmos. Environ., 31, 2649-2655, https://doi.org/10.1016/S1352-2310(96)00228-2, 1997.

Lutz, A., Mohr, C., Le Breton, M., Lopez-Hilfiker, F. D., Priestley, M., Thornton, J. A., and Hallquist, M.: Gas to Particle Partitioning of Organic Acids in the Boreal Atmosphere, ACS Earth Space Chem., 3, 1279-1287, https://doi.org/10.1021/acsearthspacechem.9b00041, 2019.

Mohr, C., Thornton, J. A., Heitto, A., Lopez-Hilfiker, F. D., Lutz, A., Riipinen, I., Hong, J., Donahue, N. M., Hallquist, M., Petäjä, T., Kulmala, M., and Yli-Juuti, T.: Molecular identification of organic vapors driving atmospheric nanoparticle growth, Nat. Commun., 10, 4442, https://doi.org/10.1038/s41467-019-12473-2, 2019.

Pande, P., Shrivastava, M., Shilling, J. E., Zelenyuk, A., Zhang, Q., Chen, Q., Ng, N. L., Zhang, Y., Takeuchi, M., Nah, T., Rasool, Q. Z., Zhang, Y., Zhao, B., and Liu, Y.: Novel Application of Machine Learning Techniques for Rapid Source Apportionment of Aerosol Mass Spectrometer Datasets, ACS Earth Space Chem., 6, 932-942, https://doi.org/10.1021/acsearthspacechem.1c00344, 2022.

Pankow, J. F.: An absorption model of gas/particle partitioning of organic compounds in the atmosphere, Atmos. Environ., 28, 185-188, https://doi.org/10.1016/1352-2310(94)90093-0, 1994.

Peräkylä, O., Riva, M., Heikkinen, L., Quéléver, L., Roldin, P., and Ehn, M.: Experimental investigation into the volatilities of highly oxygenated organic molecules (HOMs), Atmos. Chem. Phys., 20, 649-669, https://doi.org/10.5194/acp-20-649-2020, 2020.

Priestley, M., Kong, X., Pei, X., Pathak, R. K., Davidsson, K., Pettersson, J. B. C., and Hallquist, M.: Volatility Measurements of Oxygenated Volatile Organics from Fresh and Aged Residential Wood Burning Emissions, ACS Earth Space Chem., 8, 159-173, https://doi.org/10.1021/acsearthspacechem.3c00066, 2024.

Ren, S., Yao, L., Wang, Y., Yang, G., Liu, Y., Li, Y., Lu, Y., Wang, L., and Wang, L.: Volatility parameterization of ambient organic aerosols at a rural site of the North China Plain, Atmos. Chem. Phys., 22, 9283-9297, https://doi.org/10.5194/acp-22-9283-2022, 2022.

Reyes-Villegas, E., Bannan, T., Le Breton, M., Mehra, A., Priestley, M., Percival, C., Coe, H., and Allan, J. D.: Online Chemical Characterization of Food-Cooking Organic Aerosols: Implications for Source Apportionment, Environ. Sci. Technol., 52, 5308-5318, https://doi.org/10.1021/acs.est.7b06278, 2018.

Roldin, P., Eriksson, A. C., Nordin, E. Z., Hermansson, E., Mogensen, D., Rusanen, A., Boy, M., Swietlicki, E., Svenningsson, B., Zelenyuk, A., and Pagels, J.: Modelling non-equilibrium secondary organic aerosol formation and evaporation with the aerosol dynamics, gas- and particle-phase chemistry kinetic multilayer model ADCHAM, Atmos. Chem. Phys., 14, 7953-7993, https://doi.org/10.5194/acp-14-7953-2014, 2014.

Ruiz-Jimenez, J., Okuljar, M., Sietiö, O. M., Demaria, G., Liangsupree, T., Zagatti, E., Aalto, J., Hartonen, K., Heinonsalo, J., Bäck, J., Petäjä, T., and Riekkola, M. L.: Determination of free amino acids, saccharides, and selected microbes in biogenic atmospheric aerosols – seasonal variations, particle size distribution, chemical and microbial relations, Atmos. Chem. Phys., 21, 8775-8790,

https://doi.org/10.5194/egusphere-2025-229
Preprint. Discussion started: 17 March 2025

https://doi.org/10.5194/acp-21-8775-2021, 2021.

Seinfeld, J. H. and Pankow, J. F.: Organic atmospheric particulate material, Annu. Rev. Phys. Chem., 54, 121-140, https://doi.org/10.1146/annurev.physchem.54.011002.103756, 2003.

Shi, H., Yang, N., Yang, X., and Tang, H.: Clarifying Relationship between PM2.5 Concentrations and Spatiotemporal Predictors Using Multi-Way Partial Dependence Plots, Remote Sens., 15, 358, https://doi.org/10.3390/rs15020358, 2023.

Shiraiwa, M. and Pöschl, U.: Mass accommodation and gas–particle partitioning in secondary organic aerosols: dependence on diffusivity, volatility, particle-phase reactions, and penetration depth, Atmos. Chem. Phys., 21, 1565-1580, https://doi.org/10.5194/acp-21-1565-2021, 2021.

Stark, H., Yatavelli, R. L. N., Thompson, S. L., Kimmel, J. R., Cubison, M. J., Chhabra, P. S., Canagaratna, M. R., Jayne, J. T., Worsnop, D. R., and Jimenez, J. L.: Methods to extract molecular and bulk chemical information from series of complex mass spectra with limited mass resolution, Int. J. Mass Spectrom., 389, 26-38, https://doi.org/10.1016/j.ijms.2015.08.011, 2015.

Stark, H., Yatavelli, R. L. N., Thompson, S. L., Kang, H., Krechmer, J. E., Kimmel, J. R., Palm, B. B., Hu, W. W., Hayes, P. L., Day, D. A., Campuzano-Jost, P., Canagaratna, M. R., Jayne, J. T., Worsnop, D. R., and Jimenez, J. L.: Impact of Thermal Decomposition on Thermal Desorption Instruments: Advantage of Thermogram Analysis for Quantifying Volatility Distributions of Organic Species, Environ. Sci. Technol., 51, 8491-8500, https://doi.org/10.1021/acs.est.7b00160, 2017.

Su, H., Cheng, Y., and Pöschl, U.: New Multiphase Chemical Processes Influencing Atmospheric Aerosols, Air Quality, and Climate in the Anthropocene, Acc. Chem. Res., 53, 2034-2043, https://doi.org/10.1021/acs.accounts.0c00246, 2020.

Thaunay, F., Clavaguéra, C., and Ohanessian, G.: Hydration of the sulfate dianion in cold nanodroplets: $SO_4^{2-}(H_2O)_{12}$ and $SO_4^{2-}(H_2O)_{13}$, Phys. Chem. Chem. Phys., 17, 25935-25945, https://doi.org/10.1039/C5CP02557E, 2015.

Tremp, J., Mattrel, P., Fingler, S., and Giger, W.: Phenols and nitrophenols as tropospheric pollutants: Emissions from automobile exhausts and phase transfer in the atmosphere, Water Air Soil Pollut., 68, 113-123, https://doi.org/10.1007/BF00479396, 1993.

Wang, D. S. and Ruiz, L. H.: Chlorine-initiated oxidation of n-alkanes under high-NOx conditions: insights into secondary organic aerosol composition and volatility using a FIGAERO-CIMS, Atmos. Chem. Phys., 18, 15535-15553, https://doi.org/10.5194/acp-18-15535-2018, 2018.

Wang, F., Yu, H., Wang, Z., Liang, W., Shi, G., Gao, J., Li, M., and Feng, Y.: Review of online source apportionment research based on observation for ambient particulate matter, Sci. Total Environ., 762, 144095, https://doi.org/10.1016/j.scitotenv.2020.144095, 2021.

Wang, X., Zhao, Y., Hu, K., Wang, J., Wang, Q., Chen, N., Zhu, B., Zhang, H.-H., and Yu, H.: Linking Precursors and Volatility of Ambient Oxygenated Organic Aerosols Using Thermal Desorption Measurement and Machine Learning, ACS ES&T Air, https://doi.org/10.1021/acsestair.4c00076, 2024.

Ye, C. S., Yuan, B., Lin, Y., Wang, Z. L., Hu, W. W., Li, T. G., Chen, W., Wu, C. H., Wang, C. M., Huang,

https://doi.org/10.5194/egusphere-2025-229
Preprint. Discussion started: 17 March 2025

S., Qi, J. P., Wang, B. L., Wang, C., Song, W., Wang, X. M., Zheng, E., Krechmer, J. E., Ye, P. L., Zhang, Z. Y., Wang, X. M., Worsnop, D. R., and Shao, M.: Chemical characterization of oxygenated organic compounds in the gas phase and particle phase using iodide CIMS with FIGAERO in urban air, Atmos. Chem. Phys., 21, 8455-8478, https://doi.org/10.5194/acp-21-8455-2021, 2021.

Ye, Q., Wang, M. Y., Hofbauer, V., Stolzenburg, D., Chen, D. X., Schervish, M., Vogel, A., Mauldin, R. L., Baalbaki, R., Brilke, S., Dada, L., Dias, A., Duplissy, J., El Haddad, I., Finkenzeller, H., Fischer, L., He, X. C., Kim, C., Kurten, A., Lamkaddam, H., Lee, C. P., Lehtipalo, K., Leiminger, M., Manninen, H. E., Marten, R., Mentler, B., Partoll, E., Petaja, T., Rissanen, M., Schobesberger, S., Schuchmann, S., Simon, M., Tham, Y. J., Vazquez-Pufleau, M., Wagner, A. C., Wang, Y. H., Wu, Y. S., Xiao, M., Baltensperger, U., Curtius, J., Flagan, R., Kirkby, J., Kulmala, M., Volkamer, R., Winkler, P. M., Worsnop, D., and Donahue, N. M.: Molecular Composition and Volatility of Nucleated Particles from alpha-Pinene Oxidation between -50 °C and +25 °C, Environ. Sci. Technol., 53, 12357-12365, https://doi.org/10.1021/acs.est.9b03265, 2019.

Yuan, Y., Chen, X., Cai, R., Li, X., Li, Y., Yin, R., Li, D., Yan, C., Liu, Y., He, K., Kulmala, M., and Jiang, J.: Resolving Atmospheric Oxygenated Organic Molecules in Urban Beijing Using Online Ultrahigh-Resolution Chemical Ionization Mass Spectrometry, Environ. Sci. Technol., 58, 17777-17785, https://doi.org/10.1021/acs.est.4c04214, 2024.

Zaveri, R. A., Easter, R. C., Shilling, J. E., and Seinfeld, J. H.: Modeling kinetic partitioning of secondary organic aerosol and size distribution dynamics: representing effects of volatility, phase state, and particle-phase reaction, Atmos. Chem. Phys., 14, 5153-5181, https://doi.org/10.5194/acp-14-5153-2014, 2014.

Zhang, Q., Jimenez, J. L., Worsnop, D. R., and Canagaratna, M.: A Case Study of Urban Particle Acidity and Its Influence on Secondary Organic Aerosol, Environ. Sci. Technol., 41, 3213-3219, https://doi.org/10.1021/es061812j, 2007.

Zhang, Z., Xu, B., Xu, W., Wang, F., Gao, J., Li, Y., Li, M., Feng, Y., and Shi, G.: Machine learning combined with the PMF model reveal the synergistic effects of sources and meteorological factors on PM2.5 pollution, Environ. Res., 212, 113322, https://doi.org/10.1016/j.envres.2022.113322, 2022.

Zhao, Y., Hu, K., Wang, J., Wang, Q., Wang, P., Chen, N., Zhu, B., Zhang, H.-H., and Yu, H.: Quantifying New Sources of Ambient Organic Aerosol and Their Roles in Particle Growth Using Oxygenated Organic Molecule (OOM) Tracers, Environ. Sci. Technol. Lett., 11, 988-995, https://doi.org/10.1021/acs.estlett.4c00536, 2024.

Zhu, X., Wang, X., and Ok, Y. S.: The application of machine learning methods for prediction of metal sorption onto biochars, J. Hazard. Mater., 378, 120727, https://doi.org/10.1016/j.jhazmat.2019.06.004, 2019.